

Perturbative corrections to photon coincidence spectroscopy

L. Horvath and B. C. Sanders

Department of Physics, Macquarie University, Sydney, New South Wales 2109,
Australia

Abstract. Photon coincidence spectroscopy is a promising technique for probing the nonlinear regime of cavity quantum electrodynamics in the optical domain, however its accuracy is mitigated by two factors: higher-order photon correlations, which contribute to an enhanced pair count rate, and non-simultaneity of emitted photon pairs from the optical cavity. We show that the technique of photon coincidence spectroscopy is effective in the presence of these effects if the quantitative predictions are adjusted to include non-simultaneity and higher-order correlations.

PACS numbers: 42.50.Ct,42.50.Dv

1. Introduction

Photon coincidence spectroscopy (PCS) provides an accurate means for detecting quantum field effects in cavity quantum electrodynamics (CQED) (Carmichael *et al.* 1996, Sanders *et al.* 1997, Horvath *et al.* 1999, Horvath and Sanders 2001). In applications of CQED to quantum information, where entanglement between the cavity field and the internal degrees of freedom of the atom passing through the cavity is central to the scheme (Turchette *et al.* 1995), PCS offers an accurate method for probing the quantum field in the cavity. In two-photon coincidence spectroscopy (2PCS), the atom-cavity system is driven by a bichromatic field (as for nonlinear spectroscopy; see Thompson *et al.* 1998), and a detector measures the two-photon coincidence rate (2PCR) in the cavity output field. Two-photon spectral peaks are expected for particular sum frequencies of the bichromatic driving field (one frequency is fixed and the other scanned across some range of frequencies). Certain two-photon spectral peaks would occur only if the quantum description of the intracavity field is valid and not occur if the intracavity field can be described by a semiclassical field theory.

In order to test the quantum description of the intracavity field, accuracy in predicting the locations of the two-photon spectral peaks is very important. The height or the width of the two-photon spectral peaks does not need to be determined by theory accurately, but the centre of the peak, as a function of scanning field frequency, is important. We consider here two effects on the shifts of these peaks: higher-order photon correlations that contribute to the 2PCR and the non-simultaneity of the photon pairs as they exit the cavity. These two cases contribute to small shifts of the 2PCR peaks but must be accounted for in establishing accurate predictions by 2PCS.

2. Master equation and two-photon count rates

In the electric-dipole and rotating-wave approximations, the Jaynes-Cummings (JC) Hamiltonian for the two-level atom (2LA) coupled to a single mode is (Jaynes and Cummings 1963)

$$H(g) = \omega(\sigma_z + a^\dagger a) + ig(a^\dagger \sigma_- - a \sigma_+), \quad (1)$$

with g a position-dependent dipole coupling strength, a and a^\dagger the annihilation and creation operators for photons in the cavity field, σ_+ , σ_- , and σ_z the 2LA raising, lowering and inversion operators, respectively, and $\hbar = 1$. Single-atom cavity QED in the optical domain (Hood *et al.* 2000, Pinkse *et al.* 2000) validates the single-atom approximation of Eq. (1). Provided that the atoms move sufficiently slowly through the cavity (Carmichael *et al.* 1996, Sanders *et al.* 1997), and the position is randomly varying, the coupling strength g is also random: hence, a coupling strength distribution $P(g)$ can be constructed (Sanders *et al.* 1997), and we assume the $P(g)$ depicted in Fig. 5 of Sanders *et al.* 1997, which applies for a single TEM₀₀ cavity mode and atoms travelling transverse to the cavity axis. The atoms first pass through a rectangular mask, centred at an antinode with size $w_0 \times \lambda/10$ (with w_0 the cavity mode

waist and λ the optical wavelength). The atoms then traverse the cavity after passing through the mask. We restrict $Fg_{\max} < g < g_{\max}$ for g_{\max} the coupling strength at an antinode along the cavity longitudinal axis and F an effective cut-off term.

The JC spectrum for the Hamiltonian (1) is depicted in Fig. 1 and the ‘dressed states’ of the atom-cavity system are designated as the lowest-energy state $|0\rangle \equiv |0\rangle_{\text{cav}} \otimes |\mathbf{g}\rangle_{\text{atom}} \equiv |0, \mathbf{g}\rangle$, and, for n a positive integer, the ‘excited’ state couplets $|n\rangle_{\pm} \equiv i/\sqrt{2}(|n-1, \mathbf{e}\rangle \pm i|n, \mathbf{g}\rangle)$, with $|n\rangle$ the Fock state of the cavity mode and $|\mathbf{g}\rangle$ ($|\mathbf{e}\rangle$) the ground (excited) state of the 2LA. Averaging over $P(g)$ yields inhomogeneous spectral broadening (due to atomic position variability).

Two-photon excitation is provided by driving the atom directly, as it traverses the cavity, with a bichromatic field $\mathcal{E}(t) = \mathcal{E}_1 e^{-i\omega_1 t} + \mathcal{E}_2 e^{-i\omega_2 t}$. The driving-field frequency ω_1 is fixed and resonantly excites $|0\rangle \longleftrightarrow |1\rangle_-$ for the subensemble $g = g_f = \omega - \omega_1$ corresponding to $P(g) = \delta(g - g_f)$. The scanning-field frequency ω_2 excites $|1\rangle_- \longleftrightarrow |2\rangle_{\pm}$ for $P(g) = \delta(g - g_f)$. Enhanced rates of photon pair detection are then sought as the scanning frequency ω_2 is varied such that $\omega_1 + \omega_2$ is resonant with some transition $|0\rangle \longleftrightarrow |2\rangle_{\pm}$ as depicted in Fig. 1.

The master equation for this system (Sanders *et al.* 1997) can be expressed as $\dot{\rho} = \mathcal{L}\rho$ for $\mathcal{L} = \mathcal{L}_{\text{eff}} + \mathcal{D} + \mathcal{J}$, i.e. a sum of a Liouville operator \mathcal{L}_{eff} , an explicit time-dependent Liouville operator \mathcal{D} and a ‘jump’ term \mathcal{J} . We introduce $\delta \equiv \omega_2 - \omega_1$ and work in the rotating picture with respect to the driving-field component ω_1 .

For $\Xi(g) = ig(a^\dagger\sigma_- - a\sigma_+)$, the effective Hamiltonian is

$$H_{\text{eff}}(g, \mathcal{E}_1) = (\omega - \omega_1)(\sigma_z + a^\dagger a) + \Xi(g) + \Upsilon(\mathcal{E}_1) - i\kappa a^\dagger a - i(\gamma/2)\sigma_+\sigma_-, \quad (2)$$

with 2κ the decay rate for the cavity, γ the inhibited spontaneous emission rate for the partially confined atom passing through the cavity, $\Upsilon(\mathcal{E}_1) = i\mathcal{E}_1(\sigma_+ - \sigma_-)$ a monochromatic 2LA driving term, and

$$\mathcal{L}_{\text{eff}}(g, \mathcal{E}_1)\rho = -i \left[H_{\text{eff}}(g, \mathcal{E}_1)\rho - \rho H_{\text{eff}}^\dagger(g, \mathcal{E}_1) \right]. \quad (3)$$

The jump term superoperator \mathcal{J} is given by $\mathcal{J}\rho = 2\kappa a\rho a^\dagger + \gamma\sigma_-\rho\sigma_+$, and $\mathcal{D}\rho = -i[\Upsilon(\mathcal{E}_2 e^{-i\delta t}), \rho]$.

Solving the master equation for $\dot{\rho}$, and accounting for atomic position variability, yields a solution

$$\bar{\rho} \equiv \int_{Fg_{\max}}^{g_{\max}} P(g)\rho(g)dg. \quad (4)$$

For a bichromatic driving field, the density matrix does not settle to a steady state value, but, in the long-time limit $t \rightarrow \infty$, the Bloch function expansion is

$$\lim_{t \rightarrow \infty} \bar{\rho}(t) = \sum_{m=0}^{\infty} \bar{\rho}_m e^{im\delta t}, \quad (5)$$

with $\bar{\rho}_m$ time-independent matrices. As the photocount integration time is expected to be long compared to the detuning δ , it is reasonable to assume that rapidly oscillating terms average out and therefore approximate $\rho(g)$ by truncating the expansion (5).

An experimental signature for entanglement is the 2PCR, which is given by the expectation value

$$w^{(2)}(t, \delta, \mathcal{E}_1) = (2\kappa)^2 \langle : n(t_0)n(t_0 + t) : \rangle, \quad (6)$$

for $n(t) \equiv a^\dagger(t)a(t)$ and ‘ $: \cdot :$ ’ referring to normal ordering. The coefficient $(2\kappa)^2$ accounts for the photon pair rate of emission from the cavity. The expectation value corresponds to a trace over $\bar{\rho}$ in Eq. (4) for some choice of $P(g)$. The 2PCR is of interest in the asymptotically large time t_0 limit, where transients disappear and t_0 is unimportant: hence the t_0 dependence on the left-hand side of Eq. (6) is ignored. The 2PCR is obtained by collecting photons over some duration, which we call the window time τ_w . Thus, the actual 2PCR is an integral, or a double integral, over t of $w^{(2)}(t, \delta, g)$, yielding an effective two-photon coincidence rate of $w^{(2)}(\delta, g)$ for a window time of τ_w . The details of the window time, and the choice of performing a single or a double integral, are fully discussed in Sec. 4. For this Section, we assume that the window time is sufficiently small that (Sanders *et al.* 1997)

$$w^{(2)}(\delta, \mathcal{E}_1) = (2\kappa)^2 \langle : n^2 : \rangle. \quad (7)$$

For 2PCS, the major obstacle to detect entanglement is the background 2PCR due to two photons of angular frequency ω_2 contributing to excitation to the second couplet, generally by off-resonant, but nonnegligible, transitions. The method for overcoming this problem is called ‘background subtraction’. In this technique, the experiment is performed twice, once with a bichromatic driving field to obtain $w^{(2)}(\delta, \mathcal{E}_1)$ and again but with a monochromatic driving field at frequency ω_2 (i.e. $\mathcal{E}_1 = 0$). The difference between the two 2PCRs, for the cases that $\mathcal{E}_1 \neq 0$ and $\mathcal{E}_1 = 0$, is given by

$$\Delta^{(2)}(\delta, \mathcal{E}_1) = w^{(2)}(\delta, \mathcal{E}_1) - w^{(2)}(\delta, \mathcal{E}_1 = 0), \quad (8)$$

which we refer to as the ‘difference-2PCR’. The 2PCR with and without background subtraction is depicted in Fig. 2, and the importance of background subtraction is apparent for the two-photon spectral peaks in the domain $|\tilde{\delta}| \leq 1$ for $\tilde{\delta} \equiv (\omega_2 - \omega)/(\omega - \omega_1)$ and $P(g) = \delta(g - g_f)$.

3. Multi-photon contributions

The emphasis thus far has been on 2PCS, with its two-photon decay process leading to an enhanced 2PCR. Although two-photon events dominate the dynamics, multi-photon effects cannot be ignored. In fact, multiphoton contributions can be used to extract signatures of transitions from higher-order couplets in the JC ladder. This method is known as multi-photon coincidence spectroscopy (Horvath *et al.* 1999).

In principle multi-photon emissions from the cavity can be distinguished from two-photon emissions, but, in practice, a photodetection system located outside the cavity, which is designed to detect two coincident photons passing through the cavity mirror, cannot distinguish between two coincident photons and the rarer case of N coincident photons with $N > 2$. In addition to the case of multi-photon emissions in the cavity

output field, there are also cases where multiple photons simultaneously exit the cavity mirror *and* exit the side of the cavity. Hence, the two-photon coincidence rate includes contributions from multiple photons emitted from the cavity as well as two photons emitted by the cavity and at least one photon leaving the side of the cavity.

3.1. Correlation Functions

In order to treat multiphoton emissions, the correlation function $w^{(2)}(t, \delta, \mathcal{E}_1)$ in Eq. (7), must be generalized to the multiphoton case $w^{(\ell)}(\mathbf{t}, \delta, \mathcal{E}_1)$, for $\ell \geq 2$ the number of photons emitted. These photoemissions take place at random times

$$\mathbf{t} = (t_1, t_2, \dots, t_{\ell-1}), \quad (9)$$

with \mathbf{t} a vector consisting of the photoemission times. Only $\ell - 1$ photoemission times are required for ℓ photoemissions, as each photoemission time is determined with respect to the time of the first photoemission which can be fixed at $t_0 = 0$. Thus, the higher contributions to the 2PCR are given by $\sum_{\ell=2}^{\infty} w^{(\ell)}(\mathbf{t}, \delta, \mathcal{E}_1)$.

A compact notation for $w^{(\ell)}$ is possible if we introduce a single notation for the number operator n corresponding to the cavity field and for the atomic inversion operator $\sigma_+\sigma_-$. We introduce the operator Θ_i , with $i \in \{0, 1\}$, and $\Theta_0 \equiv n$, $\Theta_1 \equiv \sigma_+\sigma_-$. By introducing the length $\ell - 2$ vector \mathbf{k} , such that each $k_i \in \{0, 1\} \forall i$, we obtain the compact expression

$$w^{(\ell)}(\mathbf{t}, \delta, \mathcal{E}_1) \equiv \sum_{\mathbf{k}} \alpha_{\mathbf{k}} \left\langle : n \cdot n(t_1) \cdot \prod_{s=2}^{\ell-1} \Theta_{k_{s-1}}(t_s) : \right\rangle, \quad (10)$$

with $\{\alpha_{\mathbf{k}}\}$ a set of real constant coefficients. The sum is over all $2^{\ell-2}$ distinct vectors

$$\mathbf{k} \in \{(0, 0, \dots, 0, 0, 0), (0, 0, \dots, 0, 0, 1), (0, 0, \dots, 0, 1, 0), \dots, (1, 1, \dots, 1, 1, 1)\}. \quad (11)$$

The operators n and $\sigma_+\sigma_-$ correspond to quantum numbers *inside* the cavity: the corresponding extra-cavity terms are $2\kappa n$ and $\gamma\sigma_+\sigma_-$. These coefficients correspond to the rates for the quantum to leave through the cavity mirror and through the side of the cavity, respectively. For each n , we introduce the multiplicative factor of 2κ , and the coefficient γ applies for each $\sigma_+\sigma_-$ in the product. Thus,

$$\alpha_{\mathbf{k}} = (2\kappa)^{\ell-K} \gamma^K \text{ for } K \equiv \sum_{i=1}^{\ell-2} k_i. \quad (12)$$

For example, let us consider $\ell = 4$. In this case

$$\begin{aligned} w^{(4)}((t_1, t_2, t_3), \delta, \mathcal{E}_1) &= (2\kappa)^2 \left\langle : n \cdot n(t_1) \cdot [(2\kappa)^2 \Theta_0(t_2) \Theta_0(t_3) \right. \\ &\quad + 2\kappa\gamma \Theta_0(t_2) \Theta_1(t_3) + 2\kappa\gamma \Theta_1(t_2) \Theta_0(t_3) \\ &\quad \left. + \gamma^2 \Theta_1(t_2) \Theta_1(t_3)] : \right\rangle. \end{aligned} \quad (13)$$

We observe that $w^{(\ell)}$ is the correlation function for two photons at the initial time t_0 and a later time t_1 , plus the set of all photons emitted from the cavity or out the side at the other times $\{t_2, t_3, \dots, t_{\ell-1}\}$.

In Sec. 4 we consider the window time τ_w in detail, but here we make the small window time assumption $\kappa\tau_w \ll 1$. Hence the \mathbf{t} dependence is negligible, and

$$w^{(n \geq 2)}(\mathcal{E}_1, \delta) = \sum_{m=0}^{n-2} (2\kappa)^{n-m} \gamma^m \langle \sigma_+^m \hat{a}^{\dagger n-m} \hat{a}^{n-m} \sigma_-^m \rangle. \quad (14)$$

Expression (14) is valid provided that the window time is small, as we assume in this Section.

3.2. Three-photon coincidence rate

In Fig. 3 the three-photon coincidence rate (3PCR) is shown for the cases $\langle a^{\dagger 3} a^3 \rangle$ and $\langle \sigma_- a^{\dagger 2} a^2 \sigma_+ \rangle$ with fixed coupling strength $g = g_f = 9\kappa$. Vertical lines depict the seven values of $\tilde{\delta}$ which would lead to on- or off-resonant excitation pathways which, after the third photon absorption, are on-resonance with either $|3\rangle_-$ or $|3\rangle_+$. These vertical lines serve as a guide to where peaks in the 3PCR may be expected. The values of $\tilde{\delta}$ for which these vertical lines occur are given by the resonance conditions

$$3\omega - \sqrt{3}g = 3\omega_1, \quad (15)$$

$$3\omega \pm \sqrt{3}g = 2\omega_1 + \omega_2, \quad \tilde{\delta} = 2 \pm \sqrt{3}g/g_f, \quad (16)$$

$$3\omega \pm \sqrt{3}g = \omega_1 + 2\omega_2, \quad \tilde{\delta} = (g_f \pm \sqrt{3}g) / 2g_f, \quad (17)$$

$$3\omega \pm \sqrt{3}g = 3\omega_2, \quad \tilde{\delta} = \pm g / \sqrt{3}g_f. \quad (18)$$

The 3PCR peaks are observed near these vertical lines, although small shifts of the peaks are evident. The reason for these peak shifts is the influence of competition between excitation pathway, as discussed in Horvath and Sanders 2001 for 2PCS. These shifts in peak positions are small and do not affect the analysis here. The total 3PCR is the weighted sum of the full and dotted curves of Fig. 3: $(2\kappa)^2(2\kappa \langle a^{\dagger 3} a^3 \rangle + \gamma \langle \sigma_+ a^{\dagger 2} a^2 \sigma_- \rangle)$.

3.3. Analysis of the three-photon count rate

In order to understand the detailed structure of Fig. 3, we modify the Liouvillean superoperator \mathcal{L} by artificially eliminating particular driving terms responsible for certain peaks.

Although a thorough examination of the peak structure in Fig. 3 requires an analysis of both rates $\langle a^{\dagger 3} a^3 \rangle$ and $\langle \sigma_+ a^{\dagger 2} a^2 \sigma_- \rangle$, an analysis of one of the two graphs is sufficient. The rationale for the peak structure is readily extended to explain the similar peak structure observed for the other rate. Without loss of generality, we choose, in this Section, to study in detail the peak structure for the 3PCR $\langle a^{\dagger 3} a^3 \rangle$. This analysis of the 3PCR structure is important in Subsection 3.4, as the 3PCR is responsible for perturbative corrections to the desired 2PCR, which provides the experimental signature of quantum field effects. In addition, the 3PCR structure could be used to identify further signatures of quantum field effects compared to the 2PCR signature alone.

The isolation of specific transitions is obtained by the following procedure. For example, let us consider the influence on the 3PCR of the $|0\rangle \longleftrightarrow |1\rangle_-$ transition. We

can write the effective Hamiltonian (2) as a matrix in the dressed-state basis. To isolate this influence, we can set the matrix elements $\langle 0 | \Upsilon(\mathcal{E}_1) | 1 \rangle_-$ and $-\langle 1 | \Upsilon(\mathcal{E}_1) | 0 \rangle$ to be zero where $\Upsilon(\mathcal{E}_1)$ is the driving term of Eq. (2). In addition the matrix elements of the driving term $\langle 0 | \Upsilon(\mathcal{E}_2 \exp(-i\delta t)) | 1 \rangle_-$ and its complex conjugate can both be set to zero. The jump term \mathcal{J} is not modified because only the driving terms and their effects are of concern in this analysis.

The result of setting the matrix element $\langle 0 | \Upsilon(\mathcal{E}_1) | 1 \rangle_-$ and its complex conjugate to zero for calculating the rate $\langle a^{\dagger 3} a^3 \rangle$ is depicted in Fig. 4(a). Similarly Fig. 4(b) shows the graph for $\langle 0 | \Upsilon(\mathcal{E}_2 \exp(-i\delta t)) | 1 \rangle_-$ and its conjugate set to zero. We observe that eliminating these two matrix elements causes a dramatic reduction of neighbouring peaks at both $\tilde{\delta} = -(\sqrt{2} - 1)$, which is depicted as peak *ii*, and $\tilde{\delta} = -(\sqrt{3} - 1)/2$, which is depicted as peak *iii* in Fig. 3. The reason for this reduction is that ω_1 corresponds to the $|0\rangle \longleftrightarrow |1\rangle_-$ transition. To understand the next step we refer to Fig. 5(b) which depicts $\langle a^{\dagger 3} a^3 \rangle$ with $\mathcal{E}_2 = 0$ for the $|1\rangle_- \longleftrightarrow |2\rangle_-$ transition. In this figure it is clear that the photon of frequency ω_2 dominates the $|1\rangle_- \longleftrightarrow |2\rangle_-$ transition. For the peak $\tilde{\delta} = -(\sqrt{2} - 1)$, this transition is on resonance, but, for the peak $\tilde{\delta} = -(\sqrt{3} - 1)/2$, the transition is slightly off-resonant.

The final contribution to the rate appears in Fig. 6(b) where the contribution of an ω_2 photon to the peaks is apparent. However, the transition $|2\rangle_- \longleftrightarrow |3\rangle_-$ for the peak $\tilde{\delta} = -(\sqrt{2} - 1)$ is not resonant, but the transition is resonant for the peak at $\tilde{\delta} = -(\sqrt{3} - 1)/2$. From the three figures 4(a), 5(b) and 6(b), we observe that the peak rate at $\tilde{\delta} = -(\sqrt{2} - 1)$ and $\tilde{\delta} = -(\sqrt{3} - 1)/2$ is overwhelmingly due to a sequence of an ω_1 photon followed by two ω_2 photon absorptions. By removing one of these three photons artificially, via setting the corresponding matrix elements of the Liouvillean to zero, the peaks at $\tilde{\delta} = -(\sqrt{2} - 1)$ and $\tilde{\delta} = -(\sqrt{3} - 1)/2$ are dramatically decreased. The excitation pathway for the peak at $\tilde{\delta} = -(\sqrt{3} - 1)/2$ may be understood in a simple way as follows. Once again setting $\mathcal{E}_1 = 0$ for the $|0\rangle \longleftrightarrow |1\rangle_-$ transition reduces the peak, not only at $\tilde{\delta} = -(\sqrt{2} - 1)$, but also for its close neighbour $\tilde{\delta} = -(\sqrt{3} - 1)/2$.

Let us now consider the increase in peak *v* of Fig. 4(a). This increase is due to a decrease in competition which arises by eliminating the $|0\rangle \longleftrightarrow |1\rangle_-$ transition due to an ω_1 photon. This competition is clear from the following analysis. From Fig. 4(d), we see that peak *v* is reduced by eliminating the ω_2 photon which drives the $|0\rangle \longleftrightarrow |1\rangle_+$ transition. Then Fig. 5(h) shows that peak *v* is also reduced by eliminating the ω_2 photon-induced $|1\rangle_+ \longleftrightarrow |2\rangle_+$ transition and, finally, the ω_2 photon is also responsible for the $|2\rangle_+ \longleftrightarrow |3\rangle_+$ transition as shown in Fig. 6(h). Therefore, removing the ω_1 photon-induced $|0\rangle \longleftrightarrow |1\rangle_-$ transition allows a greater population to occur in the $|1\rangle_+$ level in Fig. 4(d) and then, via two more ω_2 -induced transition, a greater rate $\langle a^{\dagger 3} a^3 \rangle$.

In Fig. 4(a) we observe that peak *vi* is completely eliminated by setting $\mathcal{E}_1 = 0$ for the $|0\rangle \longleftrightarrow |1\rangle_-$ transition. We can see from Figs. 5(d) and 6(h) that an $\omega_1 \longleftrightarrow \omega_2 \longleftrightarrow \omega_2$ pathway exists for $|0\rangle \longleftrightarrow |1\rangle_- \longleftrightarrow |2\rangle_+ \longleftrightarrow |3\rangle_+$, which is responsible for peak *vi* in the rate $\langle a^{\dagger 3} a^3 \rangle$. A second, less important, pathway is evident in Figs. 5(b) and 6(d) as the $\omega_1 \longleftrightarrow \omega_2 \longleftrightarrow \omega_2$ induced pathway $|0\rangle \longleftrightarrow |1\rangle_- \longleftrightarrow |2\rangle_- \longleftrightarrow |3\rangle_+$. Thus,

there are two contributing pathways, one via $|2\rangle_-$ and the other via $|2\rangle_+$, which are both prevented by eliminating the ω_1 photon-induced $|0\rangle \longleftrightarrow |1\rangle_-$ transition. Therefore, the peak in Fig. 4(a) is reduced for the condition that the $|0\rangle \longleftrightarrow |1\rangle_-$ is suppressed.

We observe in Fig. 3 that peak *iv* is suppressed for peak $\tilde{\delta} = 2 - \sqrt{3}$. This involves a resonant excitation to $|1\rangle_-$ by an ω_1 photon followed by an ω_2 photon exciting to $|2\rangle_-$ with a detuning of $(1 + \sqrt{2} - \sqrt{3})g_f \doteq 0.68g_f$ followed by an ω_1 resonant excitation to $|3\rangle_-$. Another dominant pathway involves a resonant excitation to $|1\rangle_-$ by an ω_1 photon followed by another ω_1 photon excitation to $|2\rangle_-$ with detuning $(2 - \sqrt{2})g_f \doteq 0.59g_f$, followed by a resonant excitation to $|3\rangle_-$.

We do not observe a peak at $\tilde{\delta} = 2 - \sqrt{3}$ because the off-resonant excitations are small in comparison to excitations near the two peaks *iii* and *v*. In contrast, peak *viii* also involves a nonresonant pathway which is similar. This pathway involves a resonant excitation to $|1\rangle_-$ by an ω_1 photon followed by another ω_1 photon excitation to $|2\rangle_-$ with detuning $(2 - \sqrt{2})g_f \doteq 0.59g_f$, followed by a resonant excitation to $|3\rangle_+$. Peak *viii* is visible because there is no major peak nearby, but its height is less than the valley height at *iv*.

To complete the analysis of 3PCR, we consider the intriguing bump on the graph in Fig. 3 near $\tilde{\delta} \doteq -0.7$. There is no vertical line in Fig. 3 at this bump because this value of $\tilde{\delta}$ does not correspond to any resonant excitation pathway. From Figs. 4(b), 5(b) and 6(b) we observe that there is a $3\omega_2$ induced excitation pathway along $|0\rangle \longleftrightarrow |1\rangle_- \longleftrightarrow |2\rangle_- \longleftrightarrow |3\rangle_-$. The frequency for the $|0\rangle \longleftrightarrow |3\rangle_-$ transition is $3\omega_2 = 3\omega - \sqrt{3}g_f$ which corresponds to $\omega_2 = \omega - g_f/\sqrt{3}$. This value of ω_2 is equivalent to setting $\tilde{\delta} = -1/\sqrt{3}$, which corresponds to the solid vertical line *i* in Fig. 3. The reason for the bump occurring at $\tilde{\delta} \doteq -0.7$ rather than at $\tilde{\delta} = -1/\sqrt{3}$ is shown in Fig. 7 and explained below.

In Fig. 7 each excitation pathway involves nonresonant transitions. In each of the three cases, the transition $|0\rangle \longleftrightarrow |1\rangle_-$ occurs on resonance ($\tilde{\delta} = -1$) or slightly off resonance ($\tilde{\delta} = -1/\sqrt{2}$ and $\tilde{\delta} = -1/\sqrt{3}$). The $\tilde{\delta} = -1$ case does not generate a large population of the $|3\rangle_-$ level, because of the significantly off resonant excitations to $|2\rangle_-$ and to $|3\rangle_-$. Similarly, the $\tilde{\delta} = -1/\sqrt{3}$ case also does not significantly populate $|3\rangle_-$ because of the large detuning from $|2\rangle_-$ compared to the homogeneous linewidth $3\kappa + \gamma/2$. The dominant pathway is thus $\tilde{\delta} = -1/\sqrt{2} \doteq -0.7$, for which the excitation is close to resonance for $|1\rangle_-$ and $|3\rangle_-$ and exactly on resonance for $|2\rangle_-$: hence the observed bump at $\tilde{\delta} \doteq -0.7$.

In Figs. 6(c) and (d) we observe that the bump at $\tilde{\delta} \doteq -0.7$ is reduced by competition with the $|2\rangle_- \longleftrightarrow |3\rangle_+$ pathway. By setting either $\mathcal{E}_1 = 0$ or $\mathcal{E}_2 = 0$ for this transition, the bump is increased. Thus, excitation along the $|0\rangle \longleftrightarrow |1\rangle_- \longleftrightarrow |2\rangle_- \longleftrightarrow |3\rangle_+$ pathway diminishes the 3PCR, and this decrease is more pronounced for $3\omega_2 > 3\omega - \sqrt{3}g_f$. Therefore, a consequence of this competition between excitation pathways to $|3\rangle_-$ and $|3\rangle_+$ is an apparent shift of the peak responsible for the bump to lower $\tilde{\delta}$.

Figures 4–6 provide sufficient information to extend the analysis above and identify

specific excitation pathways to determine which contributions dominate the 3PCR graph of Fig. 3. The cases discussed above are illustrative examples. Also a similar analysis can be applied to understand the structure of the 3PCR $\langle \sigma_+ a^{\dagger 2} a^2 \sigma_- \rangle$, but we do not perform this analysis here.

3.4. Difference two-photon count rate

The background subtraction discussed in Section 2 is relevant to multiphoton contributions. The difference-2PCR is constructed in the same way as before, except that the multi-PCR is taken into account:

$$\Delta^{(n)}(\delta, \mathcal{E}_1) = w^{(n)}(\delta, \mathcal{E}_1) - w^{(n)}(\delta, \mathcal{E}_1 = 0). \quad (19)$$

The 2PCR contains contributions from all higher-order terms; thus, when one of the two chromatic components in the bichromatic driving field is shut off, the difference-PCR includes subtraction of all higher-order correlation functions.

It is convenient and reasonable to neglect higher-order multiphoton contributions to the 2PCR and retain only the term of interest $w^{(2)}$ and the lowest-order correction term $w^{(3)}$. Thus, the 2PCR in the perturbative limit can be approximated by $w^{(2)} + w^{(3)}$.

The difference-2PCR is depicted in Fig. 8 as a plot of $\Delta^{(2)}$ versus $\tilde{\delta}$, including the 3PCR contribution. After background subtraction, we observe 2PCR peaks for $\tilde{\delta} = 1 - \sqrt{2}$, $\tilde{\delta} = \sqrt{2} - 1$ and $\tilde{\delta} = \sqrt{2} + 1$, depicted as peaks II, III, and V, respectively. These three peaks have been identified and discussed in detail in Carmichael *et al.* 1996 and in Sanders *et al.* 1997. The important point in Fig. 8 is that the 2PCR without 3PCR corrections, in Sanders *et al.* 1997, corresponds closely to the corrected version here. That is, the solid and dotted lines in Fig. 8 are quite similar. Therefore, 3PCR would not destroy the desired peak in 2PCR. However, three-photon effects are manifested on the 2PCR peak in Fig. 8, and this extra structure is of interest. This noticeable extra structure occurs for values of $\tilde{\delta}$ corresponding to the vertical lines I, IV and VI.

The extra structure due to 3PCR is not surprising. This is because 2PCR requires excitation to $|2\rangle_{\pm}$ with zero detuning in order to observe the best possible 2PCR. This condition of excitation to $|2\rangle_{\pm}$ is also the prerequisite for observing 3PCR, as resonant excitation to $|2\rangle_{\pm}$ ensures a nonnegligible population of $|3\rangle_{\pm}$.

A particularly significant 3PCR effect is the enhancement of the peak at $\tilde{\delta} = -(\sqrt{2} - 1)$ and a slight shift in the peak position. In Fig. 8 we can compute the 2PCR with and without the 3PCR correction. The 3PCR correction term is significant. This 3PCR contribution applies for values of $\tilde{\delta}$ which contribute to peaks *ii* and *iii* in Fig. 3. Although Fig. 3 applies only for $g = g_f$, this represents the dominant contribution after background subtraction. Therefore, Fig. 3 is a useful guide for understanding the enhancement of peak II in Fig. 8.

Minor peaks occur at $\tilde{\delta}$ values for vertical lines IV and VI in Fig. 8. The origin of the peak IV is the same pathway responsible for peak *vi* in Fig. 3. Similarly, peak VI corresponds to peak *viii* in Fig. 3. The peaks in Fig. 3 enable us to understand the extra structure of the 2PCR in Fig. 8. A quantum trajectory simulation of the 2PCR,

which included the 3PCR corrections, multiple atom effects and finite window times, is shown in Fig. 5 of Carmichael *et al.* 1996. Peak IV is slightly discernible in Fig. 5 of Carmichael *et al.* 1996 although subject to a small shift in the peak position (shifts in peak position have been discussed in Horvath and Sanders 2001). The information in Subsection 3.3 enables a complete understanding of the structure in Fig. 8 and, in practice, the enhanced 2PCR in Fig. 5 of Carmichael *et al.* 1996.

4. Non-simultaneity of photodetections

In the following analysis we investigate the appropriate window time for counting photon pairs. The higher-order correlations can be ignored in determining the optimal window time τ_w as the correction for this optimal time will be small. Photon pair emissions, which arise due to de-excitation from the $|2\rangle_{\pm}$ level to the ground state of the JC ladder, are not emitted from the cavity simultaneously due to the randomness of photoemission due to the cavity linewidth. The detection of a photon pair thus depends on identifying a window time τ_w such that, for two photons detected with temporal separation $t < \tau_w$, the two photons are deemed to be members of a pair. If $t > \tau_w$, the photons are deemed to be independent single photons (not members of a pair). Here we determine the optimal window time τ_{opt} which maximises the counting rate of genuine pairs relative to the rate of false pair counts.

4.1. The two-photon count rate

The 2PCR can be obtained in more than one way. Ideally one would have a perfectly efficient photodetector that detects all photons leaving one cavity mirror. The photodetector would then provide a complete record of photon emissions from the cavity as a function of t . A perfect coincidence then arises as two simultaneously detected photons at some time t . However, there are two challenges. One challenge is that there does not exist a perfectly efficient photodetector. Therefore, some pairs of photons are observed as single-photon emissions because one member of the pair escapes observation. In fact some pairs are missed altogether because both photons escape detection. The other challenge concerns the detection of two simultaneously created photons. Although created simultaneously, the emission from the cavity is not simultaneous due to the randomness of the emission time resulting from the nonzero cavity lifetime κ^{-1} .

We consider two photons to be coincident provided that they arrive within the window time interval τ_w . The choice of window time is not obvious, and it is our aim here to determine what the window time should be. As the two simultaneous photons can be separated by a time of order κ^{-1} , as discussed above, the window time τ_w might be expected to be on the order of κ^{-1} . However, our purpose here is to consider the choice of τ_w in detail and to identify the optimal choice of window time τ_w that will produce the strongest 2PCR.

The choice of optimal window time is further complicated by the method of detecting nearly simultaneous photons. In the ideal case discussed above of a perfect photodetector yielding a record of all photon emissions from the cavity, one can then define a two-photon event as taking place if a second photon arrives between times t_0 and $t_0 + \tau_w$, *conditioned* on a photodetection at time t_0 . We refer to this rate as the *conditional* difference-2PCR and define this rate to be

$$\Delta_{\text{con}}^{(2)}(\delta, \mathcal{E}_1, \tau_w) \equiv \lim_{t_0 \rightarrow \infty} \frac{1}{\tau_w} \int_{t_0}^{t_0 + \tau_w} dt \Delta^{(2)}(t, \delta, \mathcal{E}_1). \quad (20)$$

for $\Delta^{(2)}(t, \delta, \mathcal{E}_1) = w^{(2)}(t, \delta, \mathcal{E}_1) - w^{(2)}(t, \delta, \mathcal{E}_1 = 0)$ with $w^{(2)}(t, \delta, \mathcal{E}_1)$ given by Eq. (6). (This conditional difference-2PCR for a window time $\tau_w = \kappa^{-1}$ was used in the quantum trajectory analysis of PCS in Carmichael *et al.* 1996).

Another natural way to measure the 2PCR is by counting all photon pairs defined as being separated by an interval less than τ_w . This 2PCR is referred to as the *unconditional* difference-2PCR and does not rely on starting the count for the second photon conditioned on detecting the first photon. The definition of the unconditional 2PCR is

$$\Delta_{\text{unc}}^{(2)}(\delta, \mathcal{E}_1, \tau_w) = \lim_{t_0 \rightarrow \infty} \frac{2}{\tau_w^2} \int_{t_0}^{t_0 + \tau_w} dt' \int_{t_0}^{t'} dt w^{(2)}(t' - t, \delta, \mathcal{E}_1). \quad (21)$$

As shown in Appendix A, this expression can be simplified to read

$$\Delta_{\text{unc}}^{(2)}(\delta, \mathcal{E}_1, \tau_w) = \frac{2}{\tau_w^2} \int_0^{\tau_w} du \int_0^u d\zeta w^{(2)}(\zeta, \delta, \mathcal{E}_1). \quad (22)$$

Both the conditional and unconditional difference-2PCR involve measuring photons and inferring whether two photons may be considered to have been ‘simultaneously emitted’. This determination is based on whether two photons arrive within a specified time interval. In the conditional case, two photons are treated as being members of the same ‘simultaneously emitted’ pair if the second follows the first by less than the time window τ_w ; in the unconditional case, they are considered to be members of a pair if the temporal separation of the photodetections is less than the time window τ_w . Both definitions are reasonable and depend on the nature of the detection scheme. The window time for the conditional difference-2PCR will always be less than for the unconditional difference-2PCR. The conditional process is more efficient, in a sense, because the detection interval is always triggered by the first photon, whereas the latter case allows part of an interval to pass even before the first photon is detected. Thus, in the unconditional case, a longer interval is required to be able to detect the first photon and then subsequently wait for the second photodetection.

We provide analytical solutions for the two extreme cases in Appendix A. The window time can be extremely long ($\kappa\tau_w \gg 1$), yielding expression (A.3), or extremely short ($\kappa\tau_w \ll 1$), yielding expression (A.4) for both conditional and unconditional 2PCR. The short window time ($\tau_w \rightarrow 0$) was the basis of the analysis of 2PCS in Sanders *et al.* 1997. In this treatment both the conditional and unconditional 2PCR at time t is approximated by $\langle : \hat{n}^2(t) : \rangle$. In the long-time limit the 2PCR is dominated by Poissonian statistics.

The choice of optimal window time τ_{opt} depends on the technique for observing two-photon coincidences, but another factor must also be considered. The purpose of 2PCS is to observe two-photon decay resonances from the combined atom-cavity system. These 2PCR peaks are shown in Fig. 2 as a function of the normalized scanning field frequency $\tilde{\delta}$. The choice of τ_w will depend on which peak is being observed. However, the best peak for observing a two-photon decay resonance occurs for $\tilde{\delta} = 1 + \sqrt{2}$.

4.2. The Peak-to-Valley Ratio (PVR)

In Fig. 2 the 2PCR peak at $\tilde{\delta} = 1 + \sqrt{2}$ resides over a background 2PCR that is largely independent of $\tilde{\delta}$. In this Section we employ the parameters $\mathcal{E}_1 = \mathcal{E}_2 = \kappa/2$ (equality of \mathcal{E}_1 and \mathcal{E}_2 helps to reduce the non-resonant two-photon absorption background as in Sanders *et al.* 1997) whereas, in Section 3, $\mathcal{E}_1 = \mathcal{E}_2/2 = \kappa/\sqrt{2}$ (as used in Carmichael *et al.* 1996). In this Section we choose lower driving field strengths which has the effect of producing smaller peak shifts than those studied in Sec. 3. For this choice of parameters, the 2PCR background is $\overline{\langle : n^2 : \rangle} \approx 2.1 \times 10^{-5}$. Let us characterise the quality of a 2PCR peak by the ratio of the peak height to the height of the background 2PCR. We can understand this figure of merit in terms of the ratio of signal to noise, where signal is the 2PCR from the desired two-photon decay events, and the background noise corresponds to two-photon decays arising from unwanted off-resonance two-quantum excitations and decay events. The peak-to-valley ratio (PVR) is determined by the height of the peak to the height of the background (or valley) 2PCR. The optimal window time $\tau_w = \tau_{\text{opt}}$ is defined such that the PVR for this 2PCR is maximal. That is, either a larger or a smaller choice of the window time would reduce the value of the PVR, thereby making the peak more difficult to discern from background events.

There are other concerns besides the PVR in choosing the window time. For example, choosing a much shorter window time could improve the PVR but also lengthen the run time of the experiment required to accumulate enough signal. In other words, the absolute height of the peak is also a matter of concern in determining the feasibility of the experiment and is determined by the allowable timescale of the experiment. The minimum height would need to be on the order of T^{-1} for T the timescale of the data collection.

The PVR is obtained numerically. The matrix continued-fraction method is used to solve the master equation to determine the peak height in Sanders *et al.* 1997. The background, or valley, is solved analytically by assuming a large detuning for the scanning field. The details are provided in appendix Appendix B.

The 2PCR for large $\tilde{\delta}$ is given by Expressions (B.2) and (B.4). The PVR for 2PCR is thus

$$\text{PVR}_\xi = \frac{\Delta_\xi^{(2)}(\tilde{\delta}, \mathcal{E}_1, \tau_w)}{\Delta_{0\xi}^{(2)}(\tau_w)} \quad (23)$$

with $\xi \in \{\text{con}, \text{unc}\}$. This convenient notation enables us to discuss both conditional and unconditional 2PCR with a single compact notation. In Fig. 9 surface plots of the

PVR vs g and τ_w reveal that the PVR increases as g decreases. This decrease is due to the background 2PCR (for $\tilde{\delta}$ large) becoming small as shown in Fig. 2, whereas the pair signal rate does not decline as quickly for decreasing g . The increase in PVR is due to the fact that the resonant frequency for the transition $|0\rangle \longleftrightarrow |1\rangle_-$ is $\omega - g$, for a particular subensemble with coupling strength g , whereas the pump field frequency is constrained to satisfy $\omega_1 = \omega - g_f$. Hence, as g decreases, the pump field drives the system more and more off resonance. Thus, the likelihood of driving the system from $|0\rangle$ to $|1\rangle_-$, followed by a photoemission, then repeating the driving $|0\rangle \longleftrightarrow |1\rangle_-$ and a second photoemission, decreases rapidly with diminishing g : hence the background 2PCR due to rapid driving to $|1\rangle_-$ from $|0\rangle$ is quite small. A lesser contribution to the 2PCR, due to $2\omega_1$ photons causing off-resonant excitation $|0\rangle \longleftrightarrow |2\rangle_-$, also diminishes rapidly for decreasing g because the excitation moves progressively further from the resonance condition. Although the 2PCR due to de-excitation from $|2\rangle_{\pm}$ decreases with diminishing g , the 2PCR for the background falls quicker thereby increasing the PVR.

As our objective is to optimise the PVR, we choose the value of τ_w which, for each g , maximises the PVR. A single peak for each g is evident in Figs. 9(a) and (b). In Fig. 10 we plot the value of the dimensionless quantity $\kappa\tau_w$ vs g which maximises the PVR. This choice of τ_w would provide the optimal PVR for 2PCS if g could be fixed. It is clear from Fig. 10 that the window time τ_w for achieving the optimal PVR is an order of magnitude smaller than κ^{-1} . The rapid decline of τ_{opt} in the vicinity of $g = g_f = 9\kappa$ is due to the driving from $|0\rangle$ to $|1\rangle_-$, followed by a photoemission, and repeating the process (as discussed above). Thus τ_w must be substantially reduced for $g \approx g_f$ in order to excise the single-photon contributions to the measured 2PCR.

Fig. 10 presents $\kappa\tau_{\text{opt}}$ vs g/κ for a range of values $0.2 \leq \gamma/\kappa \leq 10.0$. The effect of varying γ/κ is to change the homogeneous linewidth particularly for the $|1\rangle_-$ level, which is important for the spurious contribution to the 2PCR, as discussed above. The rapid decline in τ_{opt} , as g approaches g_f , varies with the choice of γ . For g small, the excitation from $|0\rangle$ to $|1\rangle_-$ by an ω_1 photon is sufficiently detuned that varying the homogeneous linewidth does not have much of the effect, hence the approximately flat curve for $\kappa\tau_{\text{opt}}$ vs g/κ in Fig. 10. However, the point of decline for $\kappa\tau_{\text{opt}}$ does depend on the homogeneous linewidth, and we observe that the decline occurs for smaller g with γ/κ large, and the decline occurs for large g as γ/κ decreases. Fig. 10 supports the earlier suggestion that the rapid oscillation between $|0\rangle$ and $|1\rangle_-$, with concomitant photoemissions, is indeed responsible for diminishing the PVR.

Fig. 10 is useful for understanding τ_{opt} , but the experimentally relevant choice of τ_{opt} is determined by taking the trace with respect to $\bar{\rho}$ in Eq. (4). Using the same $P(g)$ as throughout this paper, we obtain the PVR for the density matrix $\bar{\rho}$. The highest PVR is plotted against $\kappa\tau_{\text{opt}}$ in Fig. 11. Fig. 11 depicts quite clearly the optimal choice τ_{opt} which maximises the PVR, and, for $\gamma/\kappa = 2$, we observe that $\kappa\tau_{\text{opt}} = 0.111$ for conditional difference-2PCR and $\kappa\tau_{\text{opt}} = 0.135$ for unconditional difference-2PCR.

Using this approach we plot $\kappa\tau_{\text{opt}}$ vs γ/κ in Fig. 12. As $P(g)$ is heavily weighted in favor of low g , the high- g decline in Fig. 10 is not so important. Hence, we observe

that τ_{opt} is relatively insensitive to the choice of γ , and the dependence is linear with correlation coefficients of -0.9983 and -0.9995 for the conditional and unconditional cases respectively. The dependence of τ_{opt} on γ is given by $\kappa\tau_{\text{opt}} = -1.4 \times 10^{-3}\gamma/\kappa + 0.11$ for the conditional difference-2PCR and $\kappa\tau_{\text{opt}} = -2.1 \times 10^{-3}\gamma/\kappa + 0.14$ for the unconditional difference-2PCR. The variation of $\kappa\tau_{\text{opt}}$ for the range of γ/κ is very small. It is clear that τ_{opt} is an order of magnitude smaller than κ^{-1} , and the dominant deleterious contribution to the difference-2PCR is the cycling $|0\rangle \longleftrightarrow |1\rangle_-$ with corresponding photoemissions.

5. Conclusions

Photon coincidence spectroscopy (Carmichael *et al.* 1996, Sanders *et al.* 1997, Horvath *et al.* 1999, Horvath and Sanders 2001) is a promising technique for observing unambiguous experimental signatures of quantum field effects in quantum electrodynamics. This quantum field signature consists of two-photon spectral peaks at certain locations (with respect to detuning between the two chromatic components of the driving field). However, the peaks are not located exactly as predicted in previous studies due to multiphoton contributions to the two-photon count rate, due to non-simultaneity of the photon pairs emitted from the cavity and due to the effect of the cavity lifetime.

We have considered these effects here. The multiphoton contributions are responsible for additional structure in the two-photon count rate peaks as shown in Fig. 8. We observe that the higher-order contributions enhance the peak heights, rather than diminish them. Although additional structure is predicted by Fig. 3, for the chosen parameters, the additional structure is negligible on the two-photon count rate peaks. The technique of 2PCS is robust against multi-photon contributions to the two-photon count rate.

Another important quantity is the detection window time τ_w . This quantity is the duration over which two photons are treated as though they originate from the same intracavity photon pair. For a separation of greater than τ_w , the photons are regarded as having been created independently. We consider two detection protocols, conditional and unconditional difference-2PCR. In each case the optimal window time is an order of magnitude smaller than the cavity lifetime due primarily to the need to reduce the $|0\rangle \longleftrightarrow |1\rangle_-$ contribution to the two-photon count rate. We also note the negligible effect of varying the inhibited spontaneous emission rate γ for the coupling strength distribution $P(g)$ which is heavily weighted in favour of low g .

These effects, namely multiphoton contributions to the pair count rate and the optimal choice of window time, are important in the design of photon coincidence spectroscopy schemes and in interpreting the results. Photon coincidence spectroscopy has been shown here to be quite robust, even with these potential deleterious effects being included in the simulations.

Acknowledgments

This project has been funded by an Australian Research Council Large Grant, an Australian Research Council Small Grant, a Macquarie University Research Grant and the Macquarie University Postgraduate Research Fund. We acknowledge the valuable assistance provided by B. Wielinga in the early stages of this research, and valuable discussions with H. J. Carmichael throughout this undertaking.

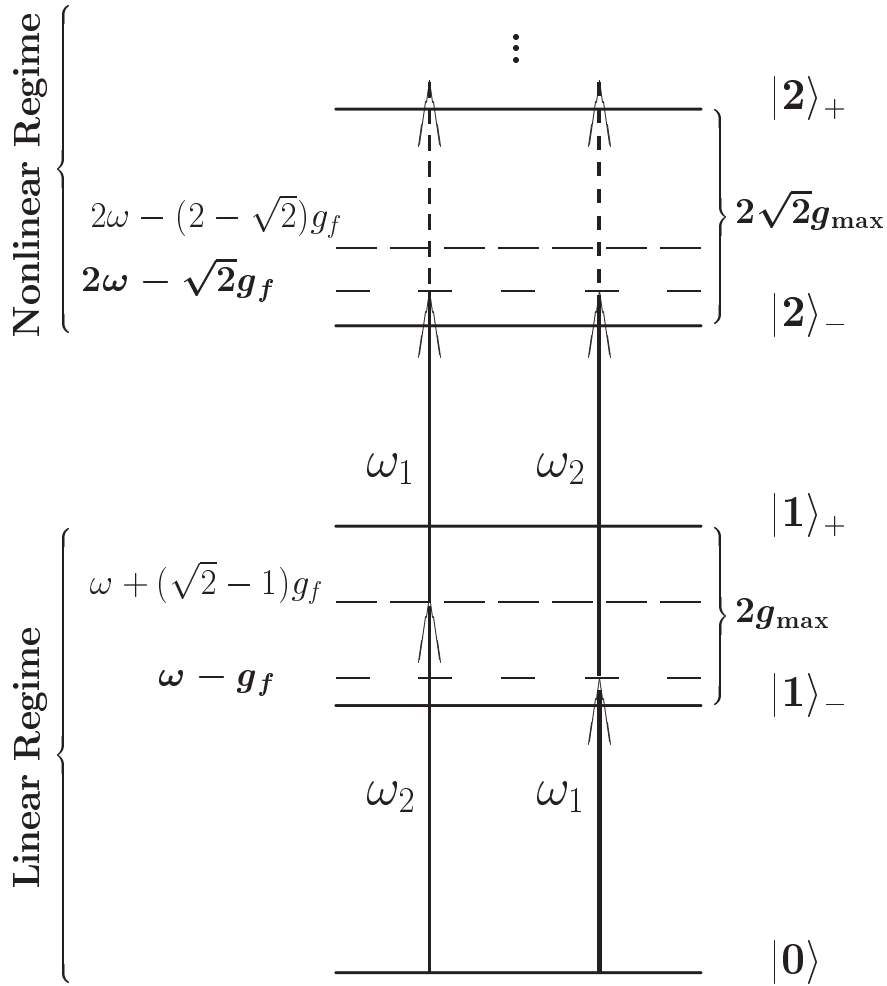


Figure 1. Two-photon excitation scheme from the ground state $|0\rangle$ to the first two excited couplets $|n\rangle_\varepsilon$ ($n \in \{1, 2\}$, $\varepsilon \in \{-, +\}$) of the dressed states. The inhomogeneous broadening of the couplets $|1\rangle_\varepsilon$ and $|2\rangle_\varepsilon$ is $2\hbar g_{\max}$ and $2\sqrt{2}\hbar g_{\max}$, respectively. Two two-photon excitations to the second couplet are depicted for a bichromatic driving field with one component of amplitude \mathcal{E}_1 and the other with amplitude \mathcal{E}_2 . The excitation pathway on the right (ω_1 then ω_2) excites resonantly from $|0\rangle$ to $|1\rangle_-$ and then may excite resonantly to either $|2\rangle_\pm$. The excitation pathway on the left (ω_2 then ω_1) excites resonantly from $|0\rangle$ to $|1\rangle_+$ to $|2\rangle_-$ for $g = (\sqrt{2} - 1)g_f$.

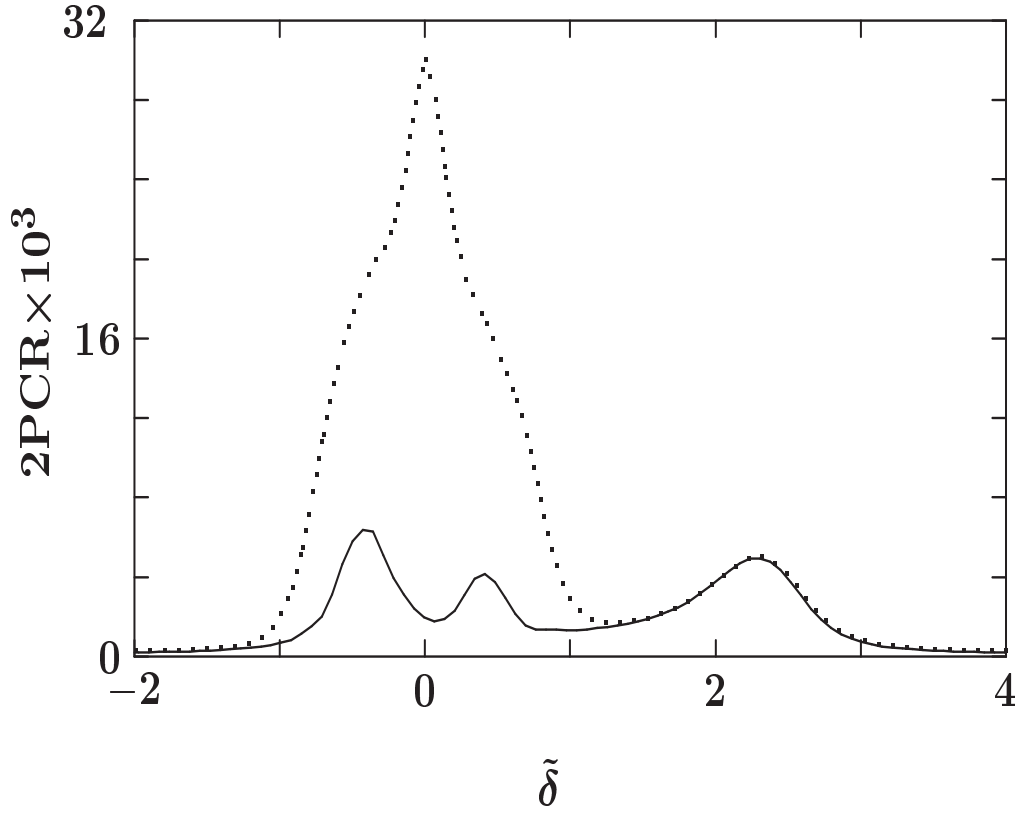


Figure 2. The 2PCR vs the normalized detuning $\tilde{\delta}$ with $\mathcal{E}_1/\kappa = 0.5$, $\mathcal{E}_2/\kappa = 0.5$, $g_f/\kappa = 9$, $\gamma/\kappa = 2$ for the inhomogeneously broadened system: $w^{(2)}(\delta, \mathcal{E}_1)$ is the solid line and $\Delta^{(2)}(\delta, \mathcal{E}_1)$ is the dashed line.

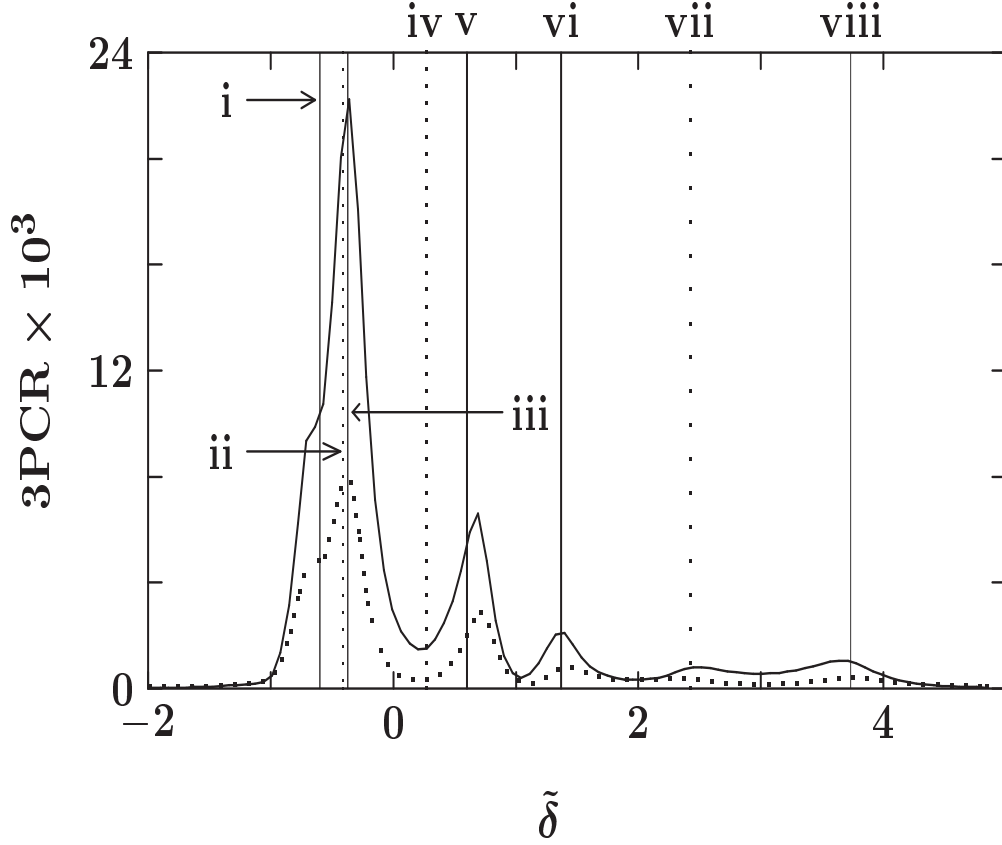


Figure 3. Three-photon count rate (3PCR) vs normalized scanning frequency for $g = g_f = 9\kappa$, $\mathcal{E}_1/\kappa = 1/\sqrt{2}$, $\mathcal{E}_2/\kappa = \sqrt{2}$ and $\gamma/\kappa = 2$. The solid line applies to $\langle a^\dagger{}^3 a^3 \rangle$, and the dotted line is for $\langle \sigma_+ a^\dagger{}^2 a^2 \sigma_- \rangle$. Alternating solid and dotted vertical lines are placed at values of $\tilde{\delta}$ for which the 3PCR peaks are expected, namely, $\tilde{\delta} \in \{-1/\sqrt{3}, -(\sqrt{2}-1), -(\sqrt{3}-1)/2, 2-\sqrt{3}, 1/\sqrt{3}, (\sqrt{3}+1)/2, \sqrt{2}+1, 2+\sqrt{3}\}$

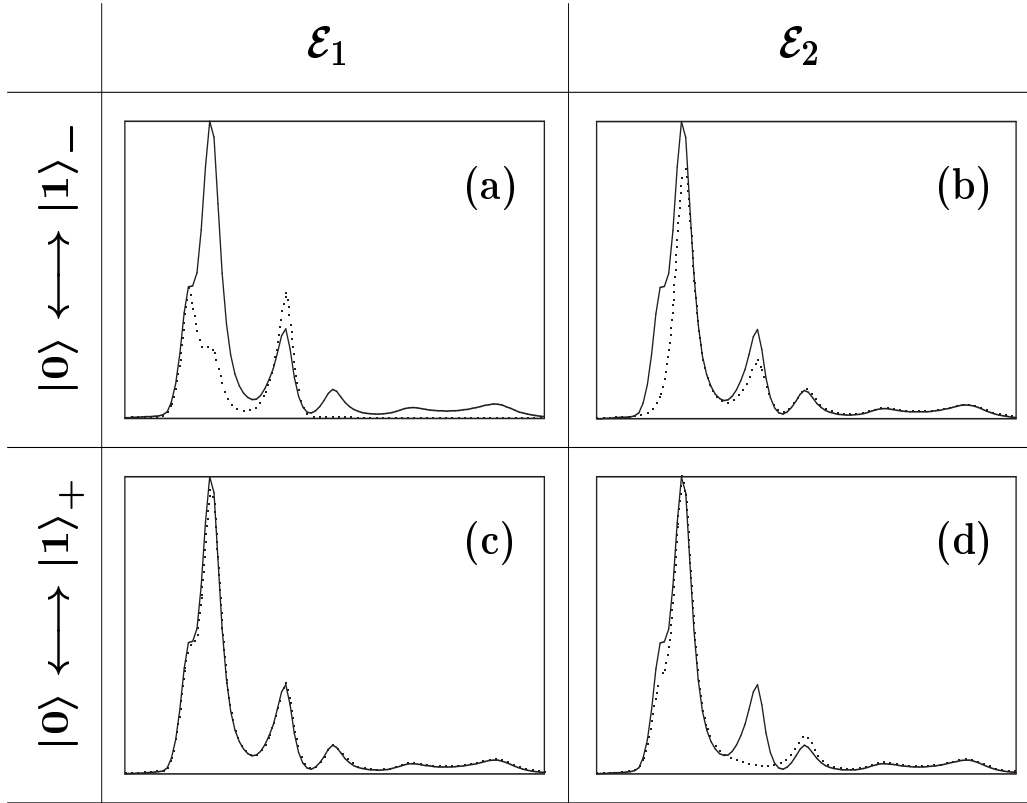


Figure 4. The rate $\langle a^{\dagger 3} a^3 \rangle$, which is depicted in Fig. 3, is reproduced here as a solid line in each of the four figures (a),(b),(c),(d). The rate $\langle a^{\dagger 3} a^3 \rangle$ is repeated as a dotted line with $\mathcal{E}_1 = 0$ for the $|0\rangle \leftrightarrow |1\rangle_-$ transition in (a), with $\mathcal{E}_2 = 0$ for $|0\rangle \leftrightarrow |1\rangle_-$ in (b), with $\mathcal{E}_1 = 0$ for the $|0\rangle \leftrightarrow |1\rangle_+$ transition in (c) and with $\mathcal{E}_2 = 0$ for the $|0\rangle \leftrightarrow |1\rangle_+$ transition in (d). We present the four figures by allocating the two rows to each of the two transitions $|0\rangle \leftrightarrow |1\rangle_{\pm}$ and the columns to whether $\mathcal{E}_1 = 0$ or $\mathcal{E}_2 = 0$ for the transition in question.

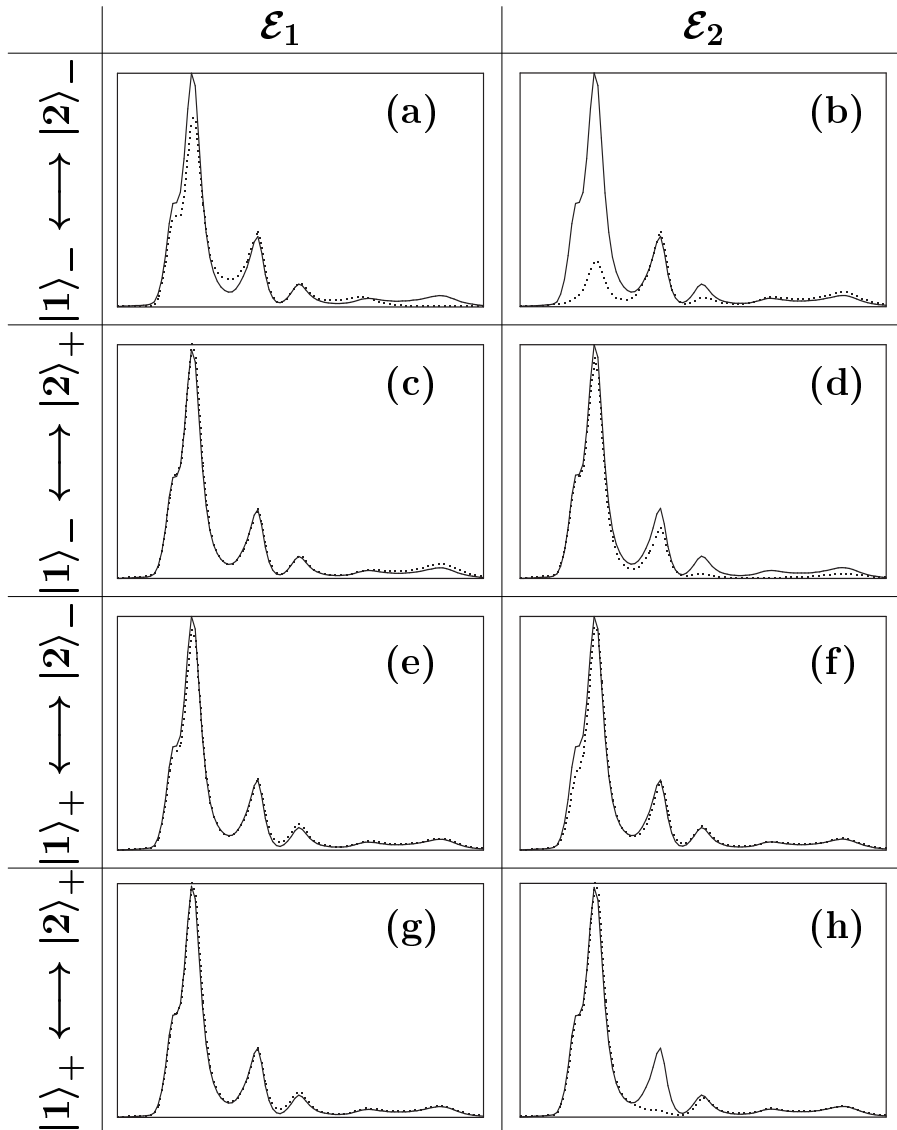


Figure 5. As for Fig. 4, with the solid line depicting the rate $\langle a^{\dagger 3} a^3 \rangle$ and the dotted line corresponding to the same rate but with either $\mathcal{E}_1 = 0$ (first column) or $\mathcal{E}_2 = 0$ (second column) for the four transitions $|1\rangle_{\varepsilon} \leftrightarrow |2\rangle'_{\varepsilon'}$ with $\varepsilon, \varepsilon' \in \{-, +\}$.

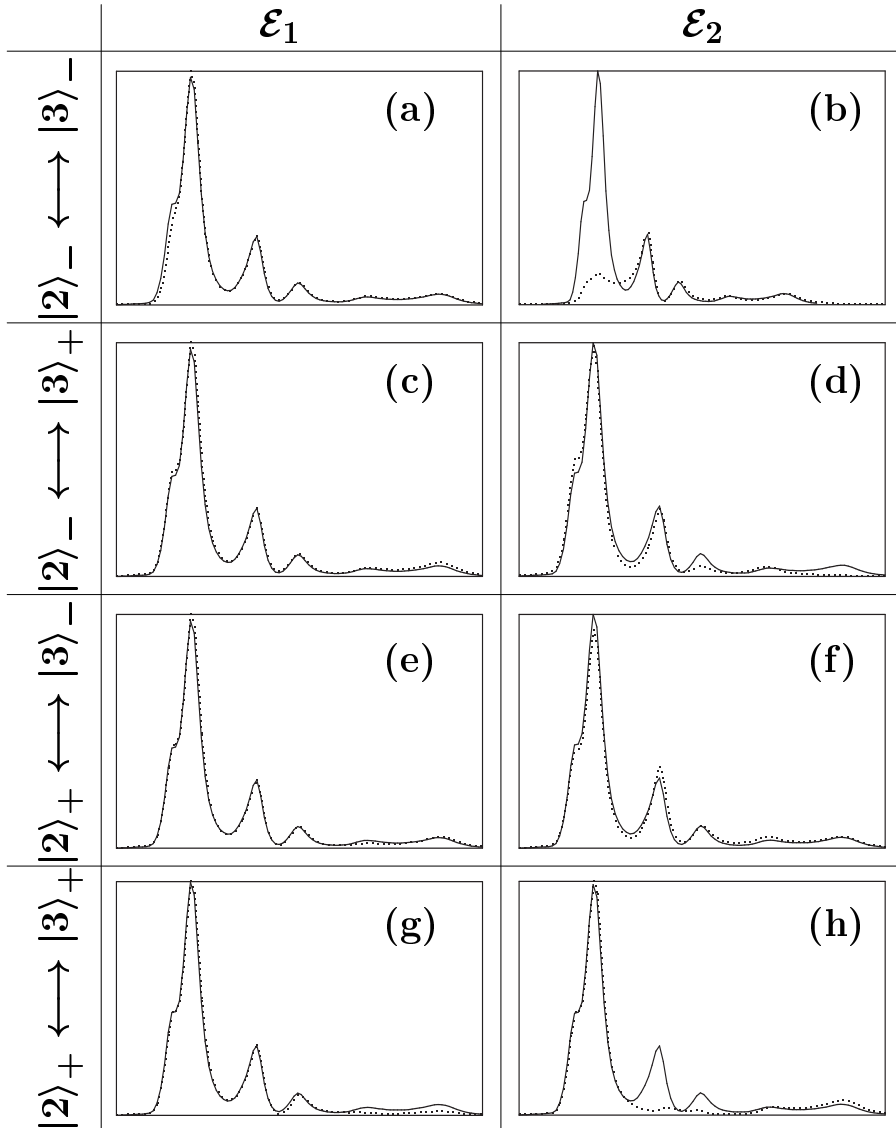


Figure 6. As for Fig. 5 but with $\mathcal{E}_1 = 0$ (first column) or $\mathcal{E}_2 = 0$ (second column) for the four transitions $|2\rangle_\varepsilon \leftrightarrow |3\rangle'_{\varepsilon'}$ with $\varepsilon, \varepsilon' \in \{-, +\}$.

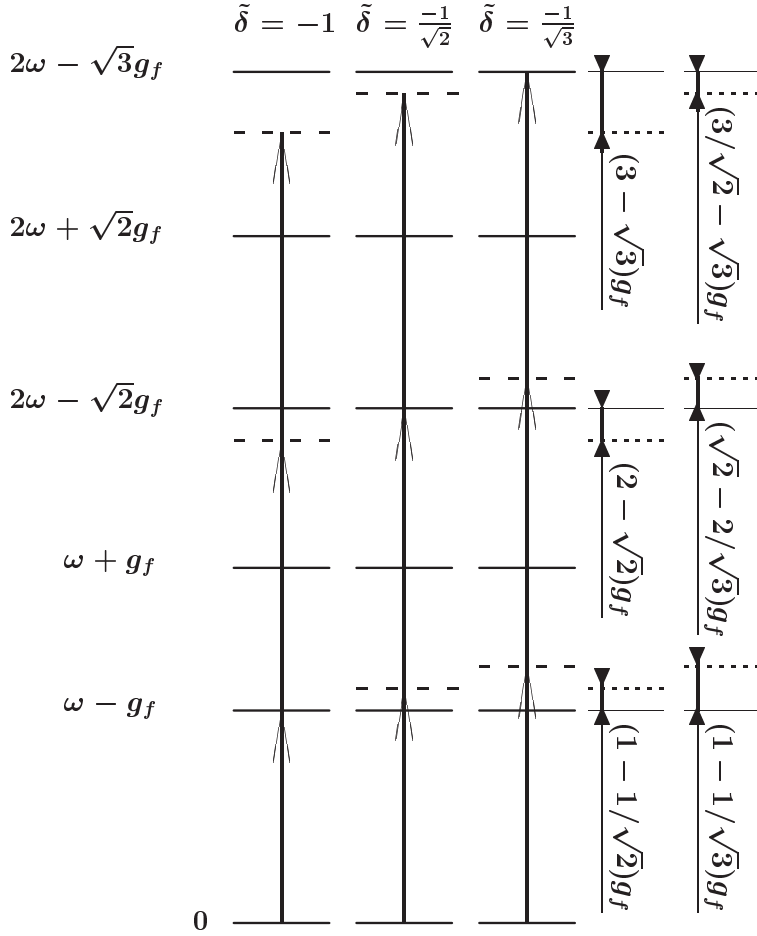


Figure 7. Excitations to $|3\rangle_-$ for $\tilde{\delta} = -1$, $\tilde{\delta} = -1/\sqrt{2}$ and for $\tilde{\delta} = -1/\sqrt{3}$ are presented here. For $\tilde{\delta} = -1$, resonant excitation occurs to $|1\rangle_-$, followed by off-resonant excitation to $|2\rangle_-$, with a detuning of $(2 - \sqrt{2})g_f \doteq 0.59g_f$, followed by off-resonant excitation to $|3\rangle_-$ with a detuning of $(3 - \sqrt{3})g_f \doteq 1.3g_f$. For $\tilde{\delta} = -1/\sqrt{2}$, off-resonant excitation from $|0\rangle$ to $|1\rangle_-$, with a detuning of $(1 - 1/\sqrt{2})g_f \doteq 0.29g_f$, is followed by a resonant excitation to $|2\rangle_-$, followed by an off-resonant excitation to $|3\rangle_-$ with a detuning of $(3/\sqrt{2} - \sqrt{3})g_f \doteq 0.39g_f$. For $\tilde{\delta} = -1/\sqrt{3}$, off-resonant excitation from $|0\rangle$ to $|1\rangle_-$, with a detuning $(1 - 1/\sqrt{3})g_f \doteq 0.42g_f$, is followed by an off-resonant excitation to $|2\rangle_-$ with a detuning of $(\sqrt{2} - 2/\sqrt{3})g_f \doteq 0.26g_f$, followed by a resonant excitation to $|3\rangle_-$.

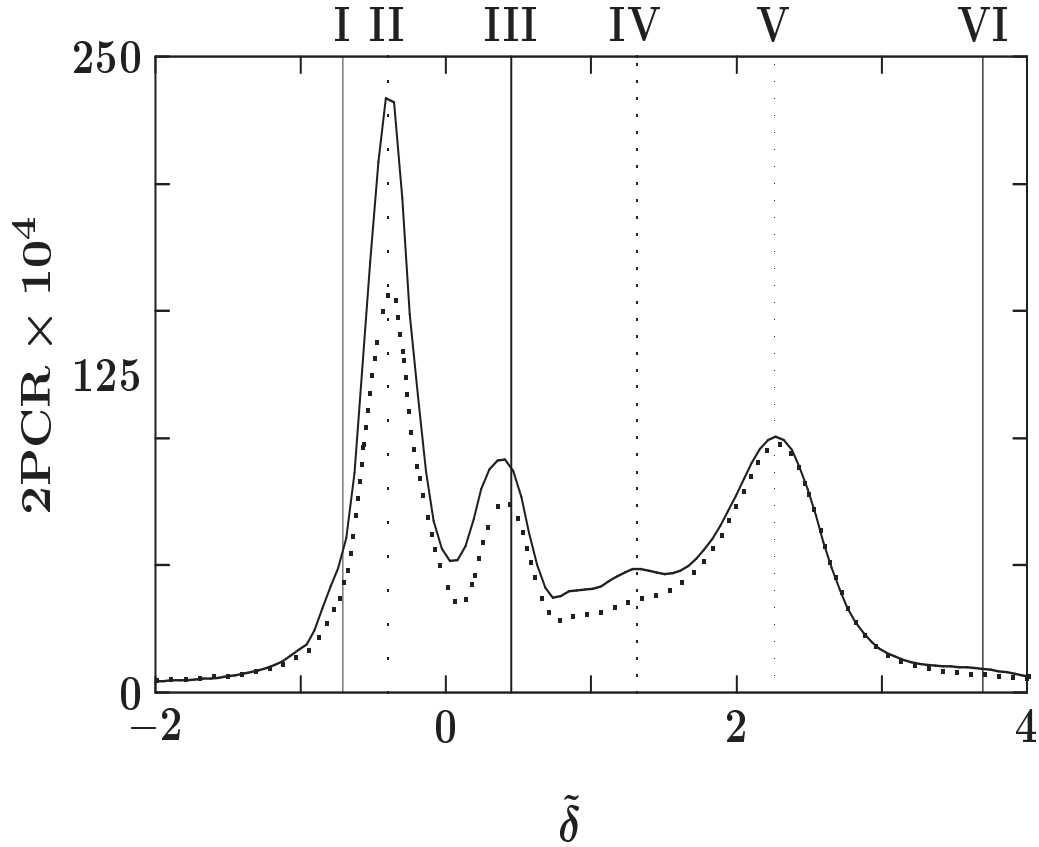


Figure 8. Difference-2PCR vs normalized scanning frequency for an inhomogeneously broadened system and $\mathcal{E}_1/\kappa = 1/\sqrt{2}$, $\mathcal{E}_2/\kappa = \sqrt{2}$, $\gamma/\kappa = 2$. The solid line corresponds to $\Delta^{(2)} + \Delta^{(3)}$ and the dotted line to $\Delta^{(2)}$.

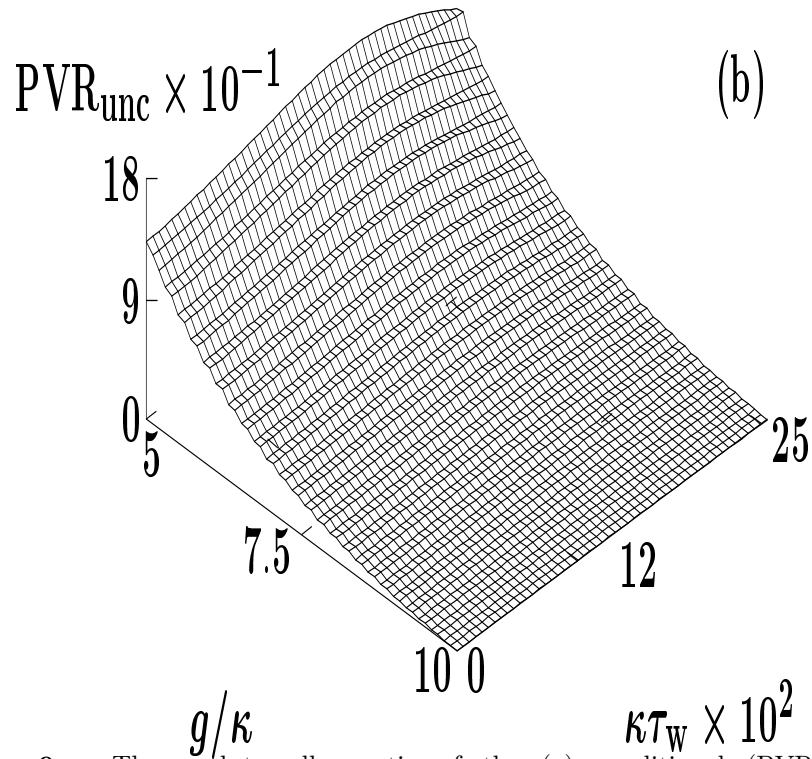
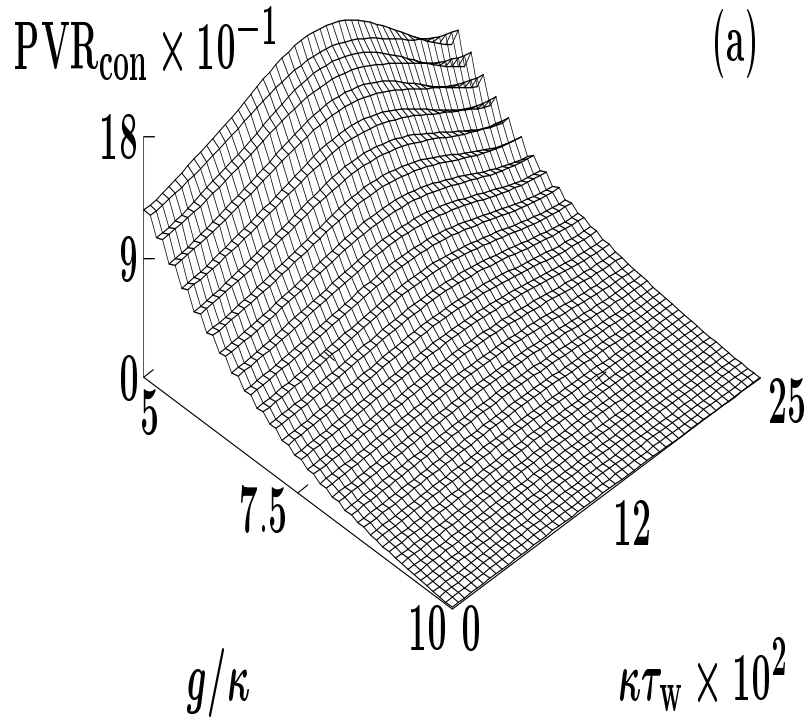


Figure 9. The peak-to-valley ratio of the (a) conditional (PVR_{con}) and (b) unconditional (PVR_{unc}) 2PCR over the scaled coupling strength g/κ and the scaled window time $\kappa\tau_w$ for the scaled loss rate $\gamma/\kappa = 2$.

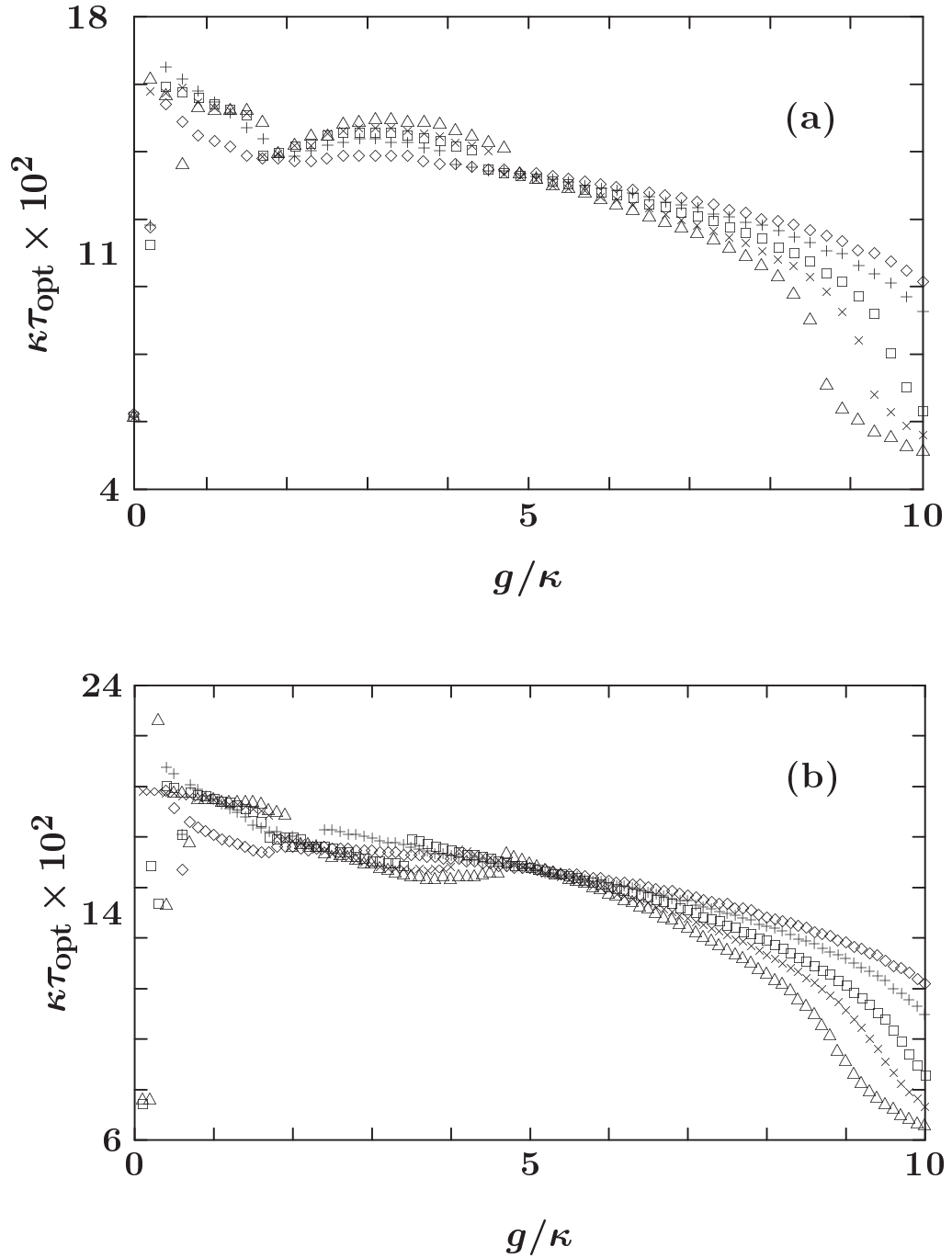


Figure 10. The scaled optimal window time $\kappa\tau_{\text{opt}}$ vs the scaled coupling strength g/κ for $\diamond \gamma/\kappa = 0.2$, $+ \gamma/\kappa = 2$, $\square \gamma/\kappa = 5$, $\times \gamma/\kappa = 7$ and $\triangle \gamma/\kappa = 10$ for (a) the conditional and (b) the unconditional 2PCR.

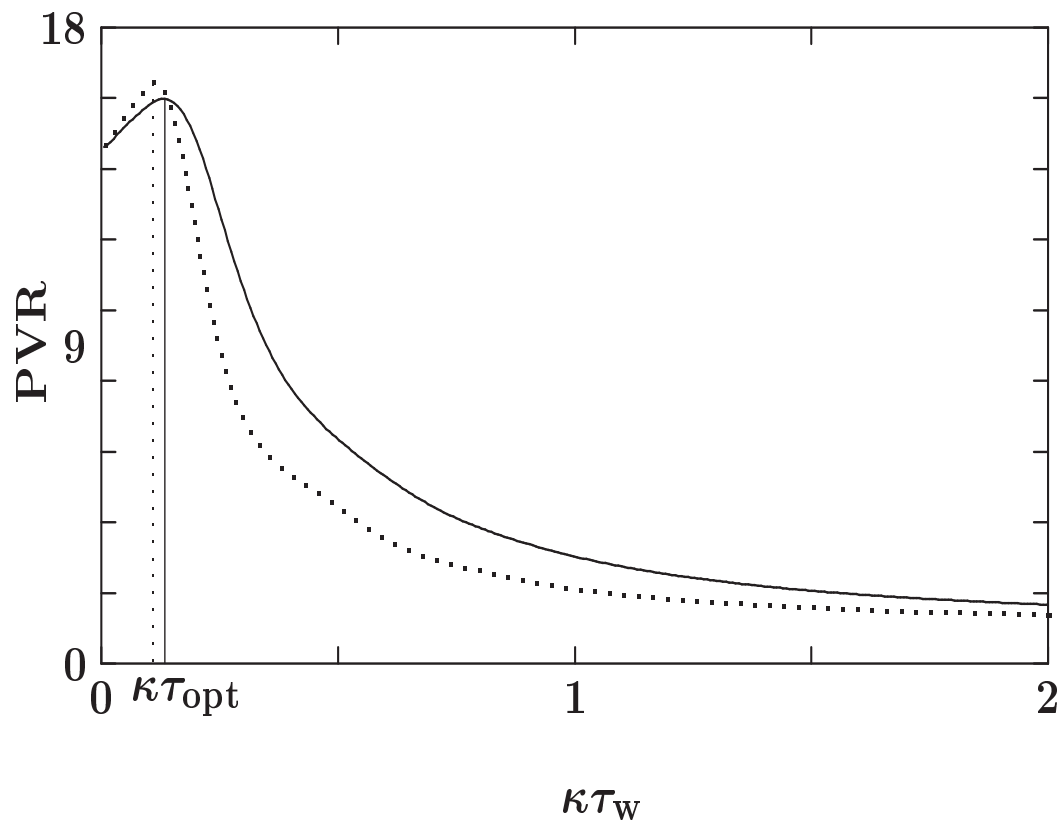


Figure 11. The peak-to-valley ratio (PVR) of the conditional (solid line) and unconditional (dashed line) 2PCR (for the masked atomic beam) vs the scaled window time $\kappa\tau_w$ for the scaled loss rate $\gamma/\kappa = 2$.

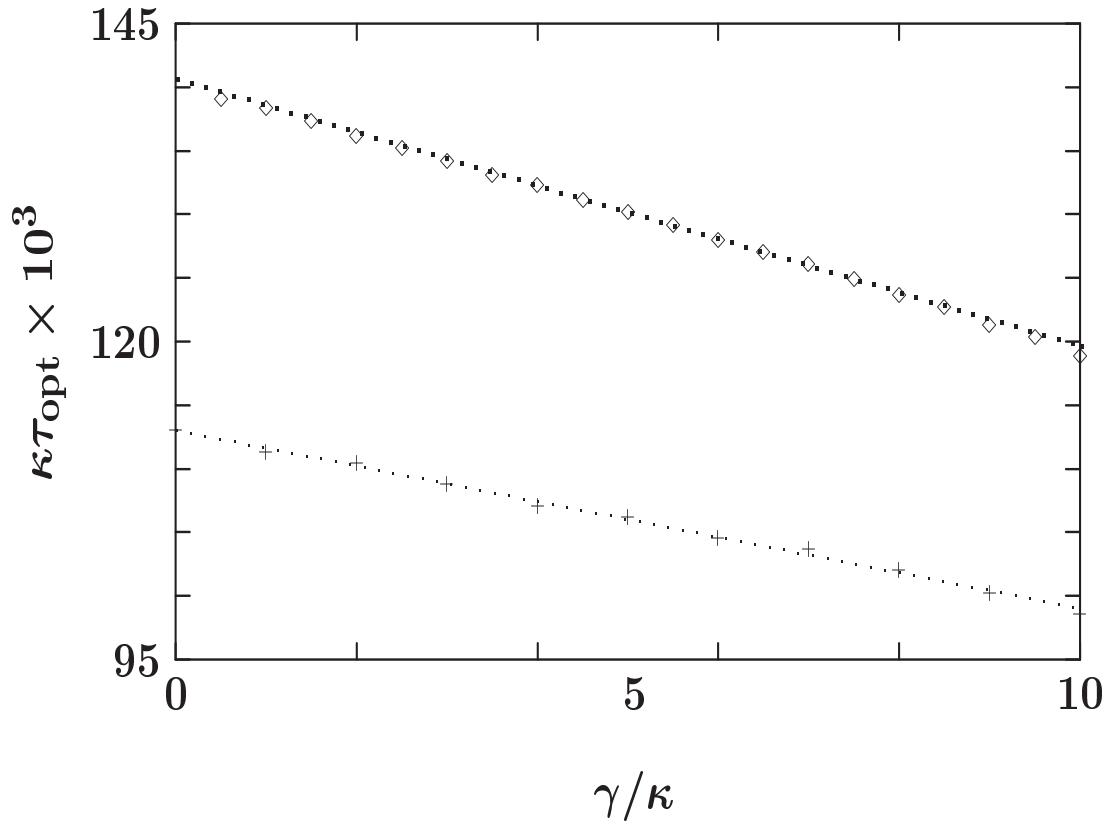


Figure 12. The scaled optimal window time $\kappa\tau_{\text{opt}}$ vs the scaled loss rate γ/κ for the masked atomic beam with inhomogeneous broadening. The symbol $+$ corresponds to the conditional τ_{opt} and \diamond to the unconditional τ_{opt} . Linear regression methods yield the two lines. For the conditional case, the slope is -1.4×10^{-3} , the intercept is 0.11, and the correlation coefficient is $r = -0.9983$. For the unconditional case, the slope is -2.1×10^{-3} , the intercept is 0.14, and the correlation coefficient is $r = -0.9995$.

Appendix A. Conditional and unconditional two-photon count rate

In the long-time limit, the conditional two-photon count rate (2PCR) is given by

$$\Delta_{\text{con}}^{(2)}(\delta, \mathcal{E}_1, \tau_w) = \frac{1}{\tau_w} (2\kappa)^2 \int_0^{\tau_w} dt \langle : \hat{n}(0) \hat{n}(t) : \rangle \quad (\text{A.1})$$

with the trace being taken over $\bar{\rho}$ in Eq. (4). If the time window τ_w is large, compared to κ^{-1} (the cavity lifetime), the two photons are highly decorrelated, and we can approximate

$$\langle : \hat{n}(0) \hat{n}(t) : \rangle \longrightarrow \langle \hat{n}(0) \rangle^2. \quad (\text{A.2})$$

Thus,

$$\Delta_{\text{con}}^{(2)}(\delta, \mathcal{E}_1, \tau_w) \longrightarrow (2\kappa)^2 \langle \hat{n}(0) \rangle^2. \quad (\text{A.3})$$

This count rate reflects the Poissonian nature of the count statistics for long window times. On the other hand, for $\kappa\tau_w \ll 1$, the correlation between photon pairs cannot be neglected. Hence, the count rate reduces to

$$\Delta_{\text{con}}^{(2)}(\delta, \mathcal{E}_1, \tau_w) \longrightarrow (2\kappa)^2 \langle : \hat{n}^2(0) : \rangle, \quad (\text{A.4})$$

which is the approximation employed in Sanders *et al.* 1997.

Similarly, in the long-time limit, the unconditional 2PCR is

$$\Delta_{\text{unc}}^{(2)}(\delta, \mathcal{E}_1, \tau_w) = \frac{2}{\tau_w^2} (2\kappa)^2 \int_0^{\tau_w} dt' \int_0^{t'} dt \langle : \hat{n}(t) \hat{n}(t') : \rangle. \quad (\text{A.5})$$

This expression can be simplified as we show below. First we make the substitution $u_{\pm} = (t' \pm t)/\sqrt{2}$. We also introduce the notation $d^2u = du_- du_+$ and let \mathcal{V} be the union of the two regions $\{0 < u_- < \tau_w/\sqrt{2}, 0 < u_+ < u_-\}$ and $\{\tau_w/\sqrt{2} < u_- < \sqrt{2}\tau_w, 0 < u_+ < \sqrt{2}\tau_w - u_-\}$

This substitution transforms the above double integral into the sum of two double integrals:

$$\begin{aligned} \Delta_{\text{unc}}^{(2)}(\delta, \mathcal{E}_1, \tau_w) &= \frac{2}{\tau_w^2} (2\kappa)^2 \int \int_{\mathcal{V}} d^2u \langle : \hat{n}(u'_-) \hat{n}(u'_+) : \rangle \\ &= \frac{2}{\tau_w^2} (2\kappa)^2 \int \int_{\mathcal{V}} d^2u \langle : \hat{n}(0) \hat{n}(\sqrt{2}u_+) : \rangle \end{aligned} \quad (\text{A.6})$$

for $u'_{\pm} = (u_+ \pm u_-)/\sqrt{2}$. The advantage of this expression is that the two-time photon number correlation depends on only one term in the double integral instead of both terms in the double integral.

Greater simplification is possible and desirable for studying the short and long window time τ_w . Substituting $u_{\pm} = w_{\pm}/\sqrt{2}$ transforms Eq. (A.6) to

$$\begin{aligned} \Delta_{\text{unc}}^{(2)}(\delta, \mathcal{E}_1, \tau_w) &= \frac{1}{\tau_w^2} (2\kappa)^2 \left[\int_0^{\tau_w} dw_- \int_0^{w_-} dw_+ \right. \\ &\quad \left. + \int_{\tau_w}^{2\tau_w} dw_- \int_0^{2\tau_w - w_-} dw_+ \right] \langle : \hat{n}(0) \hat{n}(w_+) : \rangle, \end{aligned} \quad (\text{A.7})$$

which reduces to

$$\Delta_{\text{unc}}^{(2)}(g, \delta, \tau_w) = \frac{2}{\tau_w^2} (2\kappa)^2 \int_0^{\tau_w} du \int_0^u dw \times \langle : \hat{n}(0) \hat{n}(w) : \rangle. \quad (\text{A.8})$$

For large ($\tau_w \gg \kappa^{-1}$) and small ($\tau_w \ll \kappa^{-1}$) window times $\Delta_{\text{unc}}^{(2)}$ reduces identically to $\Delta_{\text{con}}^{(2)}$ as shown in equations (A.3) and (A.4).

Appendix B. Background of conditional and unconditional 2PCR

For the scanning field far off resonance (δ large), the time-dependent component of the Liouvillian \mathcal{L} can be ignored in the rotating picture. Thus, in the rotating picture, the master equation can be written as $\dot{\rho} = \mathcal{L}\rho$ with \mathcal{L} time-independent. The coupling strength g is fixed quantity, and averaging over $P(g)$ (the inhomogeneous broadening case) is not considered in this appendix. If ρ is expressed as a vector, then \mathcal{L} can be expressed as a complex matrix with $\{-\lambda_n | n \in \mathcal{Z}_{N^2}\}$ the set of eigenvalues for N the number of levels in the Jaynes-Cummings ladder retained after truncation, and $\text{Re}(\lambda_n) \geq 0$. The density matrix can be approximated by the sum

$$\rho(t) = \sum_{n=1}^{N^2} \rho_n e^{-\lambda_n(t-t_0)} \quad (\text{B.1})$$

for $\{\rho_n\}$ a set of time-independent $N \times N$ matrices. Thus, the conditional 2PCR (20) can be written as

$$\begin{aligned} \Delta_{0\text{con}}^{(2)}(\tau_w) &= c_0 + \frac{1}{\tau_w} \int_0^{\tau_w} dt \times \sum_{n=1}^{N^2} c_n \exp[-\lambda_n t] \\ &= c_0 + \sum_{n=1}^{N^2} \frac{c_n}{\mu_n} \{1 - e^{-\mu_n}\}, \end{aligned} \quad (\text{B.2})$$

with $\mu_n \equiv \lambda_n \tau_w$ and $\lambda_n \neq 0$ for $n > 0$. Here the subscript 0 on the left-hand side of Eq. (B.2) is used to designate that we are considering the case of a monochromatic driving field. In the long window time limit,

$$c_0 = \lim_{\tau_w \rightarrow \infty} \Delta_{0\text{con}}^{(2)}(\tau_w). \quad (\text{B.3})$$

Expansion (B.2) provides a useful method for calculating $\Delta_{0\text{con}}^{(2)}(\tau_w)$ by diagonalising the Liouvillian superoperator for the monochromatically-driven case. The function $\Delta_{0\text{con}}^{(2)}(\tau_w)$ is monotonically increasing because $\partial \Delta_{0\text{con}}^{(2)} / \partial \tau_w > 0$ if $\tau_w \rightarrow \infty$. Thus, $\partial \Delta_{0\text{con}}^{(2)} / \partial \tau_w \rightarrow 0$ as the function approaches the limit given by Eq. (B.3).

In the same way, the unconditional 2PCR can be obtained:

$$\begin{aligned} \Delta_{\text{unc}}^{(2)}(\tau_w) &= c_0 + \frac{2}{\tau_w^2} \int_0^{\tau_w} du \int_0^u dw \\ &\times \sum_{n=1}^{N^2} c_n \exp[-\lambda_n w] \end{aligned}$$

$$= c_0 + 2 \sum_{n=1}^{N^2} \frac{c_n}{\mu_n} \left\{ \frac{e^{-\mu_n} - 1}{\mu_n} + 1 \right\}. \quad (\text{B.4})$$

In the $\tau_w \rightarrow \infty$ limit, $\Delta_{0\text{unc}}^{(2)}(\tau_w) \rightarrow c_0$. This is the same value for the background difference-2PCR as obtained for the conditional 2PCR. In summary, the Liouvillean superoperator is diagonalised. The master equation is solved in the $\tau_w \rightarrow \infty$ limit to obtain $\rho_{\text{ss}} = \rho(t \rightarrow \infty)$. Then $c_0 = (2\kappa)^2 \text{Tr}(a^{\dagger 2} a^2 \rho_{\text{ss}})$. This quantity is the background 2PCR for both the conditional and unconditional difference-2PCRs.

References

- Carmichael H J, Kochan P and Sanders B C 1996 *Phys. Rev. Lett.* **77** 631–4
 Hood C J, Lynn T W, Doherty A C, Parkins A S and Kimble H J 2000 *Science* **287** 1447
 Horvath L and Sanders B C 2001 *Phys. Rev. A* **63** 053812
 (—2001 *Preprint* quant-ph/011079)
 Horvath L, Sanders B C and Wielinga B F 1999 *J. Opt B: Quantum and Semiclassical. Opt.* **1** 446–51
 Jaynes E T and Cummings F W 1963 *Proc. IEEE* **51** 89
 Pinkse P W H, Fischer T, Maunz P and Rempe G 2000 *Nature* **404** 365
 Sanders B C, Carmichael H J and Wielinga B F 1997 *Phys. Rev. A* **55** 1358–70
 Thompson R J, Turchette Q A, Carnal O and Kimble H J 1998 *Phys. Rev. A* **57** 3084
 Turchette Q A, Hood C J, Lange W, Mabuchi H and Kimble H J 1995 *Phys. Rev. Lett.* **75** 4710